

**Titre:** Epitaxially stabilized thin films of  $\epsilon$ -Fe<sub>2</sub>O<sub>3</sub> (001) grown on YSZ (100)  
Title:

**Auteurs:** Lucas Corbellini, Christian Lacroix, Catalin Harnagea, Andreas Korinek, Gianluigi A. Botton, David Ménard, & Alain Pignolet  
Authors:

**Date:** 2017

**Type:** Article de revue / Article

**Référence:** Corbellini, L., Lacroix, C., Harnagea, C., Korinek, A., Botton, G. A., Ménard, D., & Pignolet, A. (2017). Epitaxially stabilized thin films of  $\epsilon$ -Fe<sub>2</sub>O<sub>3</sub> (001) grown on YSZ (100). Scientific Reports, 7. <https://doi.org/10.1038/s41598-017-02742-9>  
Citation:

**Document en libre accès dans PolyPublie**  
Open Access document in PolyPublie

**URL de PolyPublie:** <https://publications.polymtl.ca/4828/>  
PolyPublie URL:

**Version:** Version officielle de l'éditeur / Published version  
Révisé par les pairs / Refereed

**Conditions d'utilisation:** CC BY  
Terms of Use:

**Document publié chez l'éditeur officiel**  
Document issued by the official publisher

**Titre de la revue:** Scientific Reports (vol. 7)  
Journal Title:

**Maison d'édition:** Springer Nature  
Publisher:

**URL officiel:** <https://doi.org/10.1038/s41598-017-02742-9>  
Official URL:

**Mention légale:**  
Legal notice:

# SCIENTIFIC REPORTS

OPEN

## Epitaxially stabilized thin films of $\epsilon$ -Fe<sub>2</sub>O<sub>3</sub> (001) grown on YSZ (100)

Luca Corbellini<sup>1</sup>, Christian Lacroix<sup>2</sup>, Catalin Harnagea<sup>1</sup>, Andreas Korinek<sup>3</sup>, Gianluigi A. Botton<sup>3</sup>, David Ménard<sup>2</sup> & Alain Pignolet<sup>1</sup>

Received: 12 December 2016

Accepted: 18 April 2017

Published online: 16 June 2017

Epsilon ferrite ( $\epsilon$ -Fe<sub>2</sub>O<sub>3</sub>) is a metastable phase of iron(III) oxide, intermediate between maghemite and hematite. It has recently attracted interest because of its magnetocrystalline anisotropy, which distinguishes it from the other polymorphs, and results in a gigantic coercive field and a natural ferromagnetic resonance frequency in the THz range. Moreover, it possesses a polar crystal structure, making it a potential ferroelectric, hence a potential multiferroic. Due to the need of size confinement to stabilize the metastable phase,  $\epsilon$ -Fe<sub>2</sub>O<sub>3</sub> has been synthesized mainly as nanoparticles. However, to favor integration in devices, and take advantage of its unique functional properties, synthesis as epitaxial thin films is desirable. In this paper, we report the growth of  $\epsilon$ -Fe<sub>2</sub>O<sub>3</sub> as epitaxial thin films on (100)-oriented yttrium-stabilized zirconia substrates. Structural characterization outlined the formation of multiple in-plane twins, with two different epitaxial relations to the substrate. Transmission electron microscopy showed how such twins develop in a pillar-like structure from the interface to the surface. Magnetic characterization confirmed the high magnetocrystalline anisotropy of our film and revealed the presence of a secondary phase which was identified as the well-known magnetite. Finally, angular analysis of the magnetic properties revealed how the presence of twins impacts their azimuthal dependence.

Nanostructures based on iron oxides are an appealing research topic within the scientific community, given the numerous applications envisioned<sup>1–3</sup>. The intrinsic magnetic properties of iron oxides, *e.g.* their high spontaneous magnetization at room temperature and high Curie temperature, make them suitable not only for general technological applications such as magnetic recording media or permanent magnets<sup>4,5</sup>, but also for applications in various fields of medicine such as drug delivery, medical diagnostics, since beyond their magnetic properties, they are also non-toxic, biodegradable, and biocompatible<sup>6–13</sup>. Moreover, they are often used as models in theoretical studies to clarify particular magnetic features typical of nanoscaled systems not observable in their bulk counterparts<sup>14</sup>. Finally, the various forms of iron oxides constitute the most common iron compounds in nature and are generally easy to synthesize.

Although not as easy to synthesize as the other polymorphs, due to its inherent instability in ambient condition (which however did not prevent Jian craftsmen to use it as a pigment more than 800 years ago)<sup>15</sup>, attention must be given to  $\epsilon$ -Fe<sub>2</sub>O<sub>3</sub>, an intermediate phase of Fe<sub>2</sub>O<sub>3</sub> between maghemite ( $\gamma$ -Fe<sub>2</sub>O<sub>3</sub>) and hematite ( $\alpha$ -Fe<sub>2</sub>O<sub>3</sub>) with a complex orthorhombic crystal structure (Fig. 1a). Epsilon ferrite has first been synthesized in 1934, when Forestier and Guilot-Guillain reported an iron(III) oxide different from  $\alpha$ -Fe<sub>2</sub>O<sub>3</sub> and  $\gamma$ -Fe<sub>2</sub>O<sub>3</sub><sup>16</sup>. Then in 1963, Schrader and Buttner<sup>17</sup>, and almost at the same time Walter-Levy and Quemeneur<sup>18</sup>, were able to synthesize the material, to measure its X-ray diffraction (XRD) pattern for the first time. Phase purity was first obtained by Trautmann and Forestier in 1965<sup>19</sup>. Indeed, due to its inherent structural and chemical instability in ambient conditions,  $\epsilon$ -Fe<sub>2</sub>O<sub>3</sub> needs to undergo size confinement, which acts as the stabilizing factor. For example, it was shown that  $\epsilon$ -Fe<sub>2</sub>O<sub>3</sub> could be synthesized in the form of nanoparticles encapsulated in a silica (SiO<sub>2</sub>) matrix by sol-gel-based methods<sup>20</sup>, or as nanowires<sup>21</sup>. These nanostructures proved to be ferromagnetic with a Curie temperature  $T_C \approx 490$  K<sup>22</sup>, and to exhibit remarkably high values of room-temperature coercive field,  $H_C \approx 20$  kOe<sup>22</sup>. The very high coercive field of  $\epsilon$ -Fe<sub>2</sub>O<sub>3</sub> nanoparticles makes them a promising material for non-volatile memories or permanent magnets, despite their lower spontaneous magnetization in comparison with maghemite and hematite.

<sup>1</sup>Centre Énergie, Matériaux et Télécommunications, INRS, 1650 boulevard Lionel-Boulet, Varennes, Québec, J3X 1S2, Canada. <sup>2</sup>Département de Génie Physique & Regroupement québécois sur les matériaux de pointe (RQMP), Polytechnique Montréal, Montréal (Québec), H3T 1J4, Canada. <sup>3</sup>Department of Materials Science and Engineering and Canadian Centre for Electron Microscopy, McMaster University, 1280 Main Street West, Hamilton, Ontario, L8S 4M1, Canada. Correspondence and requests for materials should be addressed to L.C. (email: [corbellini@emt.ins.ca](mailto:corbellini@emt.ins.ca))

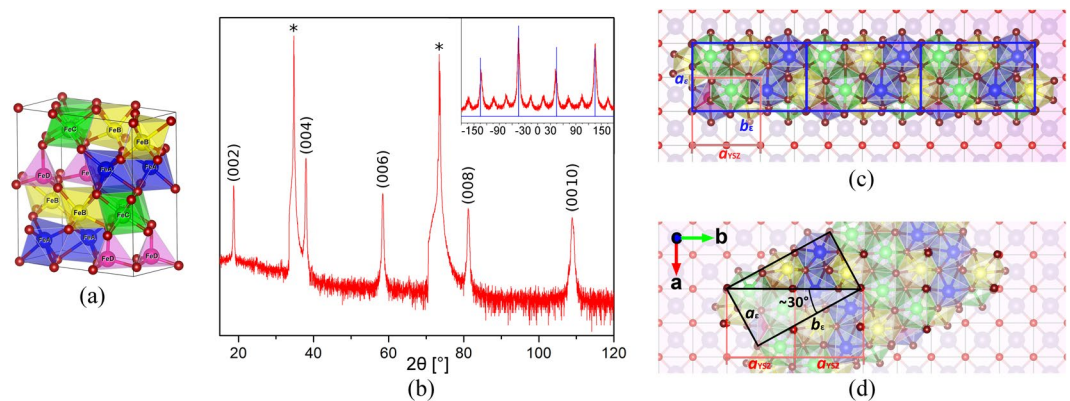


**Figure 1.** Graphic simulation of (a)  $\epsilon$ - $\text{Fe}_2\text{O}_3$  unit cell, (c) and (d) the two epitaxial matches between  $\epsilon$ - $\text{Fe}_2\text{O}_3$  (001) and YSZ (100) along with the directions of the lattice directions for YSZ. (b) X-ray  $\theta/2\theta$  diffractogram of Epsilon Ferrite thin film grown on YSZ (100), confirming the epitaxial growth. The peaks noted by asterisk are the (100) and (200) peak of the YSZ substrate. In the inset,  $360^\circ$  Phi scan for the (013) peak of  $\epsilon$ - $\text{Fe}_2\text{O}_3$  (red line), along with the scan of the (220) peak of the substrate (blue), giving evidence of the formation of twinning in-plane.

X-ray magnetic circular dichroism showed that the large coercivity of  $\epsilon$ - $\text{Fe}_2\text{O}_3$  nanoparticles originates from the presence of a large magnetocrystalline anisotropy<sup>23</sup>. This large magnetocrystalline anisotropy, induced by the lattice distortions of the  $\text{Fe}^{3+}$  coordination polyhedra, leads to a strong hybridization between the  $\text{Fe}_{3d}$  and the  $\text{O}_{2p}$  orbitals, resulting in a non-zero orbital magnetic moment  $L$ , which, through spin-orbit coupling, defines a magnetic-easy axis. Later, first principle calculations supported the experimental finding, predicting that the magnetic easy axis lies along the crystal  $a$  axis direction<sup>24</sup>.

Due to its high magnetocrystalline anisotropy, epsilon ferrite is one of the few materials having its natural ferromagnetic resonance (FMR) frequency in the THz range ( $\sim 0.1$ – $100$  THz) frequency above  $100$  GHz, thus at room temperature (without applying any magnetic field). This feature is of interest considering that THz frequencies have recently received a lot of attention both in terms of fundamental physics and applications in various fields, such as communications, defense/security, medical imaging, biology and astronomy<sup>25–29</sup>. Moreover, since  $\epsilon$ - $\text{Fe}_2\text{O}_3$  is characterized by an orthorhombic crystal structure belonging to the non-centrosymmetric and polar space group  $Pna2_1$  (Fig. 1a), it should exhibit at least pyroelectricity, which would make it a new member of the family of magneto-electric oxides<sup>30</sup>, or even a new room temperature multiferroic oxide. Finally, it has been recently shown how epsilon ferrite is also a very efficient catalyst for the sunlight-activated hydrogen generation from solutions of water and oxygenates<sup>31</sup>.

In order to integrate  $\epsilon$ - $\text{Fe}_2\text{O}_3$  into solid-state devices, nanoparticles are usually not the most suitable form. Notably, deposition of a mixture of supported  $\epsilon$ - $\text{Fe}_2\text{O}_3$  and  $\beta$ - $\text{Fe}_2\text{O}_3$  nanorods on silicon wafer has been reported, synthesized by chemical vapor deposition<sup>32</sup>. However, these nanostructures do not possess the same functional properties as their nanoparticle counterparts; in particular, they exhibit a much lower coercive field. Moreover, they do not exhibit a completely ordered structure, making them unsuitable for applications where such order is needed. In order to favor integration of  $\epsilon$ - $\text{Fe}_2\text{O}_3$  into devices and to take advantage of the magnetic, and possibly ferroelectric order(s) characterizing epsilon ferrite, the most suitable form would be *epitaxial* thin films. Recently, growth of such epitaxial epsilon ferrite thin films by pulsed laser deposition (PLD) has been reported<sup>33</sup>, whereby the metastable epsilon phase stabilization was accomplished by taking advantage of the epitaxial strain induced by the single crystal strontium titanate ( $\text{SrTiO}_3$ ) substrate. Growth on substrates other than  $\text{SrTiO}_3$ , namely alumina and yttrium stabilized zirconia (YSZ), has been recently achieved, although not directly on YSZ, but with a  $50$  nm thick buffer layer of  $\text{GaFeO}_3$  (GFO) on top of YSZ used to promote the growth of epsilon ferrite<sup>34</sup>. Moreover, although the ferroelectric behavior of single epsilon ferrite films has never been investigated, presence of reversible spontaneous polarization was recently reported in a layered structure of  $\text{SrTiO}_3/\text{Nb}/\text{AlFeO}_3/\text{SrRuO}_3/\epsilon\text{-Fe}_2\text{O}_3$ <sup>34</sup>.

In this work, we report the growth of  $100$ -nm-thick epitaxially stabilized epsilon ferrite thin films deposited *directly* on single crystalline  $100$ -oriented yttrium stabilized zirconia (YSZ) using pulsed laser deposition (PLD), without the need of a  $\text{GaFeO}_3$  buffer layer, in contrast to previous studies<sup>35</sup>. YSZ(100) single crystalline substrates were chosen since they proved to promote the epitaxial growth of  $\text{GaFeO}_3$  (GFO)<sup>36</sup>, which is isostructural to  $\epsilon$ - $\text{Fe}_2\text{O}_3$ . In addition, the growth of epitaxial YSZ films on Si(100) is possible and well documented<sup>37–39</sup>, making it a very relevant choice of substrate for future application of  $\epsilon$ - $\text{Fe}_2\text{O}_3$  epitaxial thin films in integrated devices. Structural characterization, comprising X-ray diffraction (XRD) and transmission electron microscopy (TEM) studies, has been carried on to confirm the epitaxial growth of the  $\epsilon$ - $\text{Fe}_2\text{O}_3$  thin films on YSZ and to determine the epitaxy relationships between the PLD-grown films and the substrate. The characterization of the magnetic properties of the epsilon ferrite films was realized using vibrating sample magnetometry (VSM) to record their magnetic hysteresis loops for various magnetic field directions and temperatures.

## Results and Discussion

The films structure was first studied by XRD. Both classical Bragg-Brentano geometry ( $\theta/2\theta$ ) and  $\phi$  ( $\varphi$ ) scans measurements were performed.  $\theta$ - $2\theta$  scan confirmed the epitaxial growth of (001)-oriented epsilon ferrite on YSZ (100) (Fig. 1b). Given the strong  $K_3$  lines signal arising from the substrate, a nickel filter was used in order to cut these peaks and have a cleaner diffractogram. Prior to utilizing the Ni filter, evidences of formation of an extra phase were recorded and the extra peaks observed were attributed to magnetite ( $\text{Fe}_3\text{O}_4$ ) (see supplementary information); given the non-epitaxial nature of the secondary phase, it is not possible, from the x-ray diffractogram, to estimate its volume relative to the main phase. It has been previously reported that in the case of GFO epitaxial films on YSZ (100) substrate, two distinct epitaxial relationships were found between GFO and YSZ<sup>36</sup>. Given the similitude between  $\text{GaFeO}_3$  and  $\epsilon\text{-Fe}_2\text{O}_3$  structures, we expected to observe a similar situation also for epsilon ferrite thin films. Such two epitaxial matches between  $\epsilon\text{-Fe}_2\text{O}_3$  and YSZ (100) are shown below in a graphical representation drawn with the software VESTA<sup>40</sup>, where we paid a special attention ensuring the best possible continuity between the oxygen octahedra and tetrahedra framework of the  $\epsilon\text{-Fe}_2\text{O}_3$  crystal structure and the oxygen octahedra framework of the substrate crystal structure: the first epitaxial match is given by the parallel alignment of the  $b_e$  lattice parameters of epsilon ferrite with the [100] and [010] directions of YSZ. While there is a good match between  $a_e$  and  $a_{\text{YSZ}}$ , resulting in a tensile strain of  $-0.58\%$  (using  $\text{strain} = a_{\text{film}} - a_{\text{sub}}/a_{\text{sub}}$ , and the lattice parameters of  $\epsilon\text{-Fe}_2\text{O}_3$  reported for nanoparticles,  $a = 5.08 \text{ \AA}$ ,  $b = 8.78 \text{ \AA}$ , and  $c = 9.47 \text{ \AA}$  as the relaxed state<sup>41</sup>, and  $a_{\text{sub}} = a_{\text{YSZ}} = 5.12 \text{ \AA}$ , as listed by the manufacturer CrysTec GmbH), the match for  $b$  is given by the so-called “3 for 5 tiling”, having  $3b_e \approx 5b_{\text{YSZ}}$  (Fig. 1c). Note that although this epitaxy relationship gives the same sets of in-plane orientations as the one given in refs 35 and 36, we believe that the “3 for 5 tiling”, is the correct description, given the much lower compressive strain of  $2.84\%$  it introduces along the  $b$  direction compared to the description proposed in refs 35 and 36, leading to a tensile strain of  $-14.2\%$ . The second match is given by the fact that the diagonal of the unit cell of  $\epsilon\text{-Fe}_2\text{O}_3$  equals approximately twice the lattice parameter  $a_{\text{YSZ}}$  of YSZ:  $\sqrt{a_e^2 + b_e^2} \approx 2a_{\text{YSZ}}$ . For such case, it is difficult to calculate the strain along  $a$  and  $b$  given the unusual epitaxial relation, but the tensile strain along the diagonal direction was calculated to be  $-0.97\%$ . In this configuration, the angle between the directions of the  $b_e$  lattice parameter with respect to the  $a_{\text{YSZ}}$  is equal to  $\alpha = \cos^{-1}(2a_{\text{YSZ}}/\sqrt{a_e^2 + b_e^2}) \approx 30^\circ$ . In both cases, the epitaxy we believe to be promoted by the continuity of the oxygen atoms framework in epsilon ferrite which align with the underlying oxygen framework of the substrate (Fig. 1d). In order to measure the three lattice parameters characterizing epsilon ferrite, and to confirm the presence of the two different twin variants of epitaxial  $\epsilon\text{-Fe}_2\text{O}_3$ , the position of peaks associated with planes non-parallel to the film surface were investigated. As explained in detail in the supplementary information, the crystallographic planes chosen for determining  $a$  and  $b$  lattice parameters ( $c$  was found easily from the main  $\theta$ - $2\theta$  scan), were the (132) and (013) planes, respectively. While little difference was found for the position of the 013 peak, a pronounced difference was found for the 132 peak. Such evidence confirmed the presence of two distinct epitaxial variants or twins as described above (see the supplementing information for further details). Moreover, in order to prove the mutual orientation of the film and the substrate,  $\phi$  scans of the peak corresponding to the (013) plane of  $\epsilon\text{-Fe}_2\text{O}_3$  were performed along with the one of the (220) plane of the substrate, as shown in the inset of Fig. 1b (and also shown in detail in the supplementing information). Such analysis firstly confirmed the formation of twins. Furthermore, it highlighted how the peaks corresponding to the parallel direction, with a  $90^\circ$  symmetry, are more intense than the non-parallel ones, which appear at circa  $\pm 30^\circ$  with respect to the parallel peaks. Very similar behavior was seen also for epitaxial thin films of GFO (001) on YSZ (100)<sup>42</sup>.

Aberration corrected Scanning Transmission Electron Microscopy (STEM) high-angle annular dark-field (HAADF) imaging further confirmed the epitaxial growth of epsilon ferrite on YSZ (100) (Fig. 2). In the image, we observed the presence of a thin buffer layer (few nanometers thick) at the interface between the substrate and the film. Considering that XRD has indicated the presence of a parasitic phase, which we ascribed to magnetite, we believe that this interfacial layer consists of magnetite. This will be further supported by the magnetic measurements, below. Moreover, the presence of multiple in-plane growth variants (twins) is observed (the areas with different contrast), which appear to form pillar-like structures. Finally, by selecting areas of a highly detailed picture belonging to different growth orientations and using Fourier transform enhancement software to improve the contrast of the image, we were able to pair the different structures observed in the twins with graphical unit cells rotated according to the epitaxial relationships with the substrate described above, thus convincingly confirming the proposed epitaxy relationship derived from XRD analysis. There appears to be reasonable agreement between the experimental observation and calculations of HAADF images (assuming a Gaussian probe as a first approximation) in the [010] projection of the structure in the red frame and [410] or  $[4\bar{1}0]$  for the green and blue frames. However, the agreement between the experimental pattern in the images and calculations (supplementary information) and projected structure shown, assuming the Fe ions are only visible in HAADF image, does not appear to be suitable for the area highlighted in the yellow frame, due to the possible overlap of two crystals in the projection of the foil. Nevertheless, such analysis helps to visualize the clear difference among the growth orientations and tries to match the different growth domain with the possible corresponding unit cell.

The magnetic properties of the films were analyzed via Vibrating Sample Magnetometry (VSM). Hysteresis loops were first recorded with the magnetic field applied both parallel (in-plane) and perpendicular (out-of-plane) to the film surface (Fig. 3a). In order to obtain solely the film signal, magnetic contributions of the sample holder (glass rod) and the substrate were measured separately and subtracted from the total signal. The strong difference in the coercive field and in the approach to saturation at the maximum applied field between the in-plane and out-of-plane measurements confirms the high magnetic anisotropy of the epsilon ferrite epitaxial films.

Temperature dependent measurement of the remanent magnetization under no field and of the magnetization with an applied magnetic field of 1000 Oe are presented in Fig. 3b. A ferromagnetic to paramagnetic transition is observed at a temperature of  $\approx 460 \text{ K}$ , which we attribute to  $\epsilon\text{-Fe}_2\text{O}_3$ . We note that the Curie



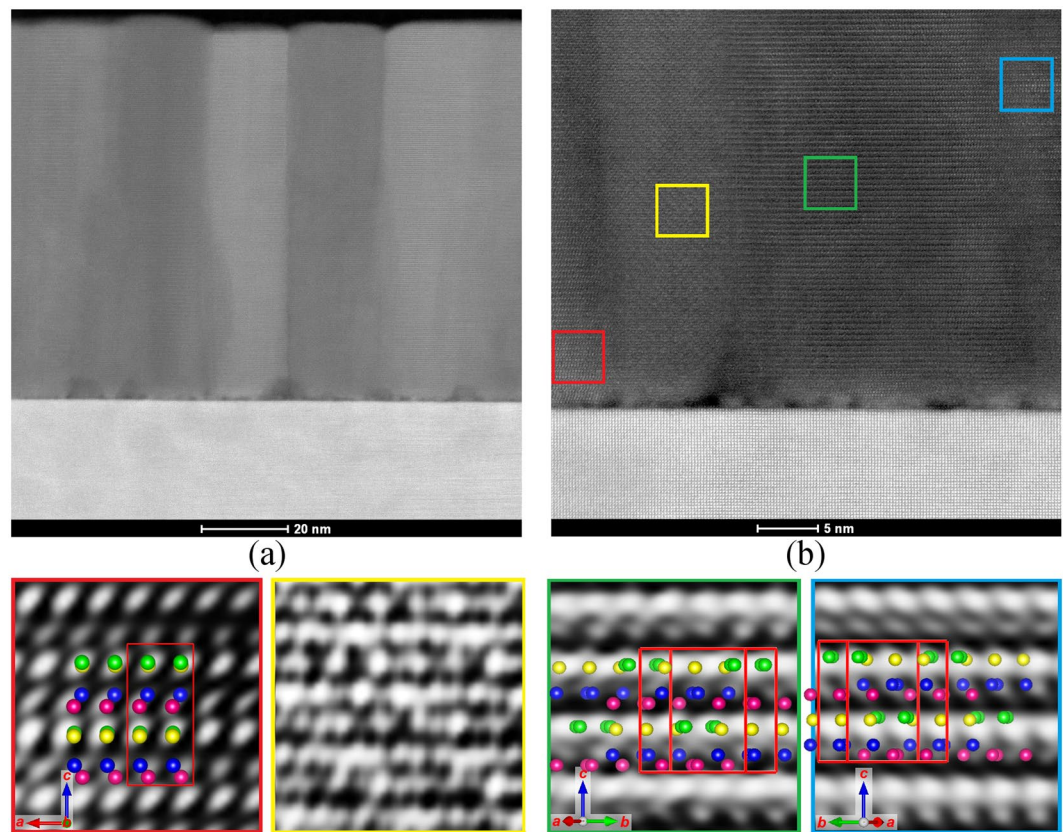


**Figure 2.** (a) STEM image of a circa 100 nm thick film of  $\epsilon$ -Fe<sub>2</sub>O<sub>3</sub> on YSZ (100) highlighting the formation of pillar-like twins, (b) detail of the interface between the substrate and the film, evidencing the formation of 'bubbles' of a foreign phase (most likely Fe<sub>3</sub>O<sub>4</sub>) at the interface. Below: high-magnification of the 4 colored selected areas overlapped with simulated  $\epsilon$ -Fe<sub>2</sub>O<sub>3</sub> structures rotated according to the proposed epitaxy relationships to further prove the existence of different growth in-plane orientation. If the orientation in the red box, with the b axis pointing out-of-plane is taken as 0°, the unit cells depicted in the other boxes are rotated, respectively by 300° (green), and 120° (light blue) (note that the 2 last unit cells (green) and (light blue) have a 180° rotational symmetry). No match was found for the yellow selection, probably due to the overlap of two different growth domains in the STEM image.

temperature  $T_C \approx 460$  K of our  $\epsilon$ -Fe<sub>2</sub>O<sub>3</sub> thin films is slightly lower than the one reported for  $\epsilon$ -Fe<sub>2</sub>O<sub>3</sub> nanoparticles ( $T_C \approx 490$  K)<sup>22</sup>. Moreover, the measurements under a small applied magnetic field of 1000 Oe, well below the coercive field of the hard magnet  $\epsilon$ -Fe<sub>2</sub>O<sub>3</sub>, but larger than the coercive field of a soft magnet, does indeed reveal the presence of a soft secondary ferromagnetic phase with a  $T_C$  higher than 550 K, consistent with the presence of some Fe<sub>3</sub>O<sub>4</sub> ( $T_C = 850$  K) observed by XRD. In contrast to some explanations reported in the literature resorting to the presence of multiple twins to explain the pinched nature of the loop, and as we will see below, the pinched nature of the hysteresis loop can be simply explained by the simultaneous presence of epsilon ferrite and magnetite. In order to determine the relative contribution of the two magnetic phases  $\epsilon$ -Fe<sub>2</sub>O<sub>3</sub> and Fe<sub>3</sub>O<sub>4</sub> to the measured magnetic hysteresis loop, we developed a method consisting in differentiating the measured loop, fitting the various peaks of the 1<sup>st</sup> derivative by using a summation of Voigt distributions in addition to a constant, deconvoluting the signals originating from the different magnetic phases (which simply correspond to the different peaks), and finally integrating exclusively and independently each Voigt functions<sup>43</sup>. Our technique, which we named D-D-SI, from "Derivative - Deconvolution - Selective Integration", allows us discriminate the various contributions originating from different magnetic phases, and also to eliminate every linear contribution due to the paramagnetic and/or diamagnetic signals arising either from the vibrating rod or/and from the substrate, along with any further linear contribution possibly coming from the film.

The reconstructed loops obtained from the D-D-SI technique are shown in Fig. 3c for the two  $\epsilon$ -Fe<sub>2</sub>O<sub>3</sub> and Fe<sub>3</sub>O<sub>4</sub> magnetic phases (red and yellow lines) and the sum of the two magnetic contributions (blue line). For comparison, the hysteresis loop obtained using the conventional way, *i.e.* by subtracting the measured contributions of the substrate and the rod from the measured signal of the thin film is also shown (blue symbols). In order to compare the two loops and demonstrate that the experimentally measured loop is well described by their sum (the small residual being a linear contribution that has not been captured in the modeling), we show the moment, as measured [emu] rather than the magnetization (moment/volume). Plotting the magnetizations in SI units [A/m] (see Figure SI 4), would make this comparison and graphical addition more difficult given the

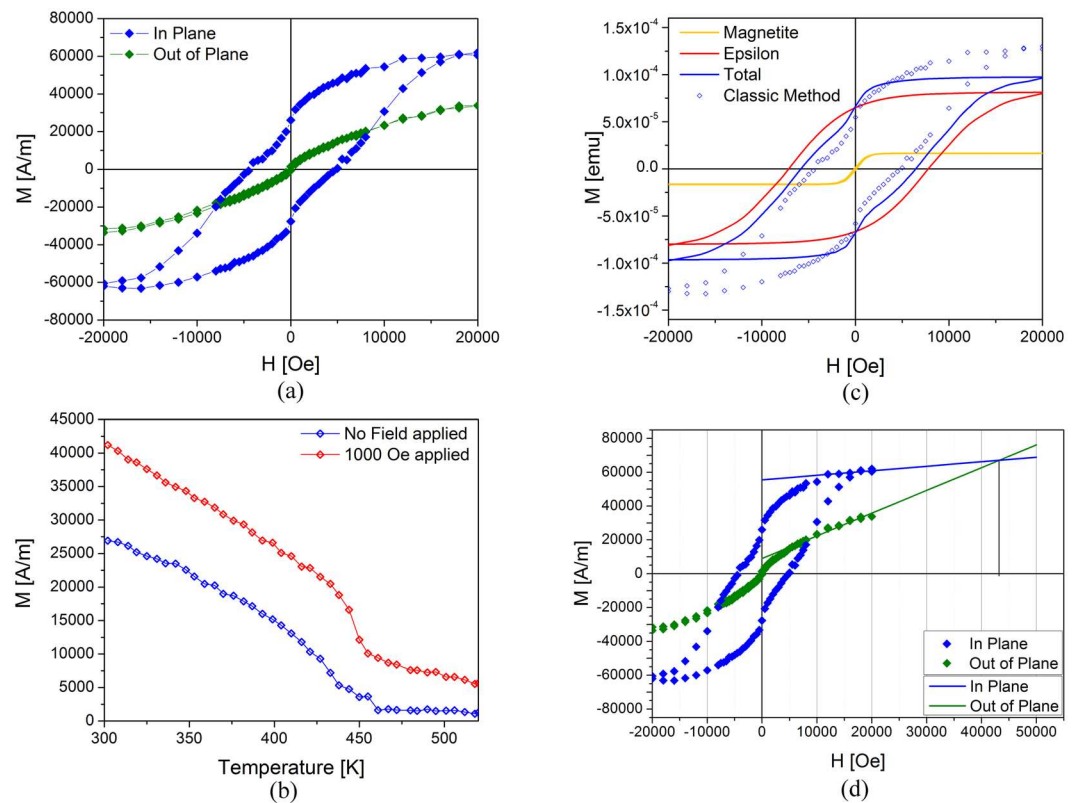


**Figure 3.** (a) Dependence of the magnetization of the  $\epsilon$ - $\text{Fe}_2\text{O}_3$  thin film with the applied magnetic field in the sample plane (blue symbols) and out of the sample plane (green symbols), showing the anisotropy of the sample. (b) Plot of M vs T measured under no field (blue) and under an applied magnetic field of 1000 Oe (red), showing how M does not vanish for temperature higher than the Curie temperature of  $\epsilon$ - $\text{Fe}_2\text{O}_3$  of 460 K when a small magnetic field is applied, thus revealing the presence of a soft phase with higher  $T_C$ . (c) Experimental (blue symbols) and analytical (blue line) substrate corrected measurement, along with the two hysteresis loops corresponding to the separation of the epsilon ferrite (red) and magnetite (yellow) phase, respectively. (d) Estimation of the anisotropy field by comparing the in-plane and out-of-plane measured hysteresis loops.

higher magnetization of magnetite compared to epsilon (3–4 times higher) and the different volumes of the soft magnetite and hard epsilon ferrite phases, which ratio was estimated to be circa 1:10. The volume ratio was found assuming the magnetite phase to be in the form of nanoclusters and its magnetization to be 309 [emu/cm<sup>3</sup>]<sup>44–48</sup>. It has to be noted that utilizing such value for magnetization, instead of the standard value for bulk magnetite of 480 [emu/cm<sup>3</sup>]<sup>49</sup> results in a higher estimation of the volume ratio (estimated to be 1:10), which would be 1:15 if the value of bulk magnetite is used. As discussed in ref. 43, the difference observed between the hysteresis loops obtained using the D-D-SI method and the hysteresis loop obtained using the conventional method corresponds to a linear contribution. This linear contribution can originate from different sources. For example, an error measurement of 7.5% on the magnetic contribution of the substrate could explain the difference<sup>43</sup>. Alternately, the difference could also be explained by the presence of ferromagnetic domains in the thin films, whose hard axis is parallel to the applied field direction.

Our results indicate that the presence of the magnetite parasitic phase, which possesses a coercive field of  $\sim 100$  Oe, has the drastic effect of reducing the coercive field of the hysteresis loop of the whole film ( $H_c \sim 5$  kOe). In comparison, the epsilon ferrite domains are individually characterized by a magnetization at saturation of  $M_s \approx 40$  kA/m and a coercive field  $H_c \approx 8$  kOe (see supplementary information for the method for determination of  $M_s$  in S.I. units). Furthermore, by extrapolating the values in the linear regime for both the in-plane and out-of-plane hysteresis, we estimated the anisotropy field to be  $\sim 43$  kOe (Fig. 3d). We note that these values are smaller than those reported in the case of epsilon ferrite nanoparticles ( $M_s \approx 15$ – $20$  emu/g, which gives  $M_s \approx 81$ – $108$  kA/m using 5.4 g/cc as density for epsilon,  $H_c \approx 20$  kOe and  $H_A \approx 65$  kOe). The lower coercivity measured can possibly be explained by the presence of multiple growth variants, each with its easy axis in a different direction, thus averaging the magnetic hysteresis loops along several magnetic easy axis. As a consequence, it is possible that our thin films are not completely saturated when subjected to a field of 20 kOe, which is the maximum field of our VSM. As a consequence, the magnetization at saturation, the coercive field and anisotropy field values obtained here can be considered as lower limits.

Finally, we note that a pinched hysteresis loop was also observed in epitaxial (001)-oriented thin films of epsilon ferrite grown on different (111)-oriented perovskites (SrTiO<sub>3</sub>, LaAlO<sub>3</sub> and LSAT) by our group (unpublished), as well as in epsilon ferrite thin films synthesized by other groups on SrTiO<sub>3</sub> (111)<sup>33,34</sup>. We note also

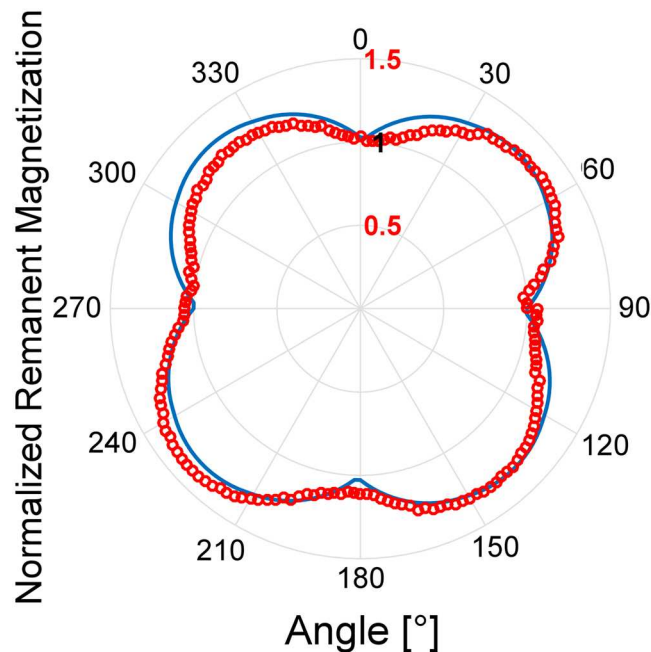


**Figure 4.** Polar plot of normalized  $M_r$  vs angle (red symbols), and the model we developed to fit the data (blue line).

that other effects may contribute to the pinched nature of the magnetic hysteresis loop, such as the presence of antiphase boundaries (APB) between the differently oriented growth domains<sup>50</sup>, where the magnetization may, for example, lie perpendicular to the film surface, or the presence of nanostructures which may grow on top of the film, as reported for  $\text{CoFe}_2\text{O}_4$  epitaxial thin films<sup>51</sup>. However, we believe that the simplest manner to explain it, overlooked so far in the published literature, is the presence of a soft magnetic phase in addition to epsilon ferrite.

The angle-dependent magnetic properties was obtained by recording in-plane hysteresis loops every 2 degrees. The in-plane angle dependence of the remanent magnetization  $M_r$  was extracted from the measured loops. To analyze the azimuthal dependence of  $M_r$ , a simple model which averages the remanence of the different growth variant parallel to the measured axis was utilized<sup>52</sup>. Such model is based on the assumption that, at zero applied field, the magnetization inside each crystal is uniform and aligned along their magnetic easy axis ( $a$ -axis). This assumption is supported by a critical dimension analysis based on the anisotropy field values and the dimensions of our epsilon ferrite crystals obtained from TEM (see Fig. 2) allowing us to infer that the crystals are essentially ferromagnetic monodomains<sup>30, 52</sup>. The angular dependence of the normalized remanent magnetization for one crystal orientation can thus be modeled by the absolute value of  $\cos(\text{angle} + \text{offset})$ . Six different contributions to the remanent magnetization were used corresponding to the six different growth variants (two “parallel” with  $b\epsilon$  aligned along the [010] and the [100] direction of the substrate, and four “non-parallel”, aligned along the [1 $\bar{1}$ 0], [4 $\bar{1}$ 0], [410], and [110]). The contribution of each variant to the total was weighted in order to fit satisfactorily the assumed data with our model (see Fig. 4). Our results indicate that the magnetic contribution of the two “parallel” variants account for the larger contribution (~93% of the total remanent magnetization), which is consistent with the data found by angular XRD (~85% of the counts, inset of Fig. 1b and supplementary information). The difference between the measured data and the model can be attributed to the non-concentric rotation of the rod holding the sample during the measurements<sup>53, 54</sup>.

Finally, using our D-D-SI method, we extracted the in-plane angular dependence of  $M_r$  for the magnetite phase. Our results show that the remanent magnetization of magnetite do not significantly varies with the angle at which the magnetic field is applied (not shown; see supplementary information).

## Conclusions

We successfully grew (001)-oriented epitaxial thin films of epsilon ferrite on single crystalline YSZ (100) via pulsed laser deposition. As seen for epitaxial thin films of  $\text{GaFeO}_3$ , isostructural to  $\epsilon\text{-Fe}_2\text{O}_3$ , YSZ (100) proved to promote two different epitaxy relationships. Moreover, due to the lower symmetry of the film in comparison to that of the substrate, the growth lead to multiple positioning or twinning, which was observed and confirmed both through x-ray diffractometry and TEM imaging. These features lead to an angular dependence of the magnetic properties that may represents an issue in uses where a single magnetic easy axis is required, like in magnetic memories. For application in such devices, epitaxial films of epsilon ferrite with a single in-plane orientation need to be grown. Nevertheless, the ability of growing  $\epsilon\text{-Fe}_2\text{O}_3$  epitaxially on YSZ (100) is of great significance, given how this material is often used as a buffer layer for the growth of oxides on top of (100)-oriented silicon wafers<sup>37–39</sup>.

Along with the desired  $\epsilon\text{-Fe}_2\text{O}_3$  phase, concomitant growth of randomly oriented magnetite was recorded both via XRD measurements and through magnetic characterization. The presence of the soft magnetic phase



‘magnetite’ correctly explains the pinched nature of the magnetic hysteresis loops measured. Data processing, allowed us to separate the contribution of the two phases from the total magnetic hysteresis. Although non-ideal, formation of a soft magnetic phase should not necessarily constitute a problem for all magnetic applications; in particular, devices based on  $\epsilon$ -Fe<sub>2</sub>O<sub>3</sub> for THz applications will not be affected given the much lower FMR frequency of the soft magnetite.

## Methods

**Growth of thin films.** The films were deposited by pulsed laser deposition utilizing a Kr excimer laser (wavelength 248 nm, pulse duration ~22 ns) with a pulse repetition rate of 5 Hz, focused on the surface of a 1 inch diameter ceramic target placed circa 5.5 cm far from the substrates with a fluence of ~1.8 J/cm<sup>2</sup> (spot size ~0.03 cm<sup>2</sup>). The target was prepared by sintering Fe<sub>2</sub>O<sub>3</sub> powders (Semiconductor Industries, 99.9% purity), resulting in a mixture of polycrystalline hematite ( $\alpha$ -Fe<sub>2</sub>O<sub>3</sub>) and amorphous Fe<sub>2</sub>O<sub>3</sub>. The thin film growth was performed at substrate temperature of 800 °C in oxidizing environment, where the O<sub>2</sub> pressure was maintained at 75 mTorr. Thickness of the films was measured by profilometer and Atomic Force Microscopy (AFM), yielding a growth rate of ~0.04 Å/pulse.

**Structural characterization.** Structural characterization was performed by X-ray diffraction using the K $\alpha$  radiation of copper ( $\lambda$  = 1.5407 Å) in a PANalytical X'Pert MRD PRO diffractometer.

Cross-sectional transmission electron microscopy samples were prepared with a Focused Ion Beam instrument (Zeiss NVision 40) with multiple milling stages at decreasing incident ion energies down to 5 keV, and a final polishing step using an Ar-beam milling using a Fischione NanoMill operated at liquid nitrogen temperatures as discussed in detail in a previous report<sup>55</sup>. This procedure has been shown to minimize damage and oxygen loss even in beam-sensitive samples.

Electron microscopy observations were carried out with an FEI-Titan 80–300 Scanning Transmission Electron Microscope (STEM) equipped with aberration correctors of the probe and imaging forming lenses, an energy loss spectrometer (Gatan Quantum model), and an electron beam monochromator. Imaging with a high-angle annular dark field detector and collection angles providing atomic-number (Z) contrast, was used to provide information on local structural arrangement, including the interface atomic structure and the presence of grain boundaries separating the crystalline grains in the films.

**Magnetic characterization.** An EV9 Vibrating Sample Magnetometer (VSM) made by ADE Technologies (MicroSense, Lowell MA, USA) was used to characterize the magnetic properties of the samples. Magnetic hysteresis loops were recorded for the epsilon ferrite thin films at room temperature with the magnetic field, varying between  $\pm 20000$  Oe, applied both parallel (in-plane) and perpendicular (out-of-plane) to the film surface.

## References

- Lu, A.-H., Salabas, E. L. & Schuth, F. Magnetic Nanoparticles: Synthesis, Protection, Functionalization, and Application. *Angew. Chem. Int. Ed.* **46**, 1222–1244 (2007).
- Wu, W., He, Q. G. & Jiang, C. Z. Magnetic Iron Oxide Nanoparticles: Synthesis and Surface Functionalization Strategies. *Nanoscale Res. Lett.* **3**, 397 (2008).
- Teja, A. S. & Koh, P.-Y. Synthesis, properties, and applications of magnetic iron oxide nanoparticles. *Prog. Cryst. Growth Charact. Mater.* **55**, 22–45 (2009).
- Gonzalez, J., Chubykalo, O. & Gonzalez, J. M. *Encyclopedia of Nanoscience and Nanotechnology*. **10**, (American Scientific Publishers, 2004).
- Cornell, R. M. & Schwertmann, U. *The Iron Oxides: Structure, Properties, Reactions, Occurrence and Uses*. (Wiley-VCH, 2003).
- Bulte, J. W. M. & Kraitchman, D. L. Iron oxide MR contrast agents for molecular and cellular imaging. *NMR Biomed.* **17**, 484–499 (2004).
- Berry, C. C. & Curtis, A. S. G. Functionalisation of magnetic nanoparticles for applications in biomedicine. *J. Phys. D Appl. Phys.* **36**, R198–R206 (2003).
- Gupta, A. K. & Gupta, M. Synthesis and surface engineering of iron oxide nanoparticles for biomedical applications. *Biomaterials* **26**, 3995–4021 (2005).
- Laurent, S. *et al.* Magnetic Iron Oxide Nanoparticles: Synthesis, Stabilization, Vectorization, Physicochemical Characterizations, and Biological Applications. *Chem. Rev.* **108**, 2064 (2008).
- Mornet, S., Vasseur, S., Grasset, F. & Duguet, E. Magnetic nanoparticle design for medical diagnosis and therapy. *J. Mater. Chem.* **14**, 2161–2175 (2004).
- Pankhurst, Q. A., Connolly, J., Jones, S. K. & Dobson, J. Applications of magnetic nanoparticles in biomedicine. *J. Phys. D Appl. Phys.* **36**, R167–R181 (2003).
- Tartaj, P., del P Morales, M., Veintemillas-Verdaguer, S., Gonzalez-Carreño, T. & Serna, C. J. The preparation of magnetic nanoparticles for applications in biomedicine. *J. Phys. D Appl. Phys.* **36**, R182–197 (2003).
- Thorek, D. L. J., Chen, A. K., Czupryna, J. & Tsourkas, A. Superparamagnetic Iron Oxide Nanoparticle Probes for Molecular Imaging. *Ann. Biomed. Eng.* **34**, 23–38 (2006).
- Dormann, J. L., Fiorani, D. & Tronc, E. In *Advances in Chemical Physics* (eds. Prigogine, I. & Rice, S. A.) **98**, 283–494 (John Wiley, 1997).
- Dejoie, C. *et al.* Learning from the past: rare epsilon-Fe<sub>2</sub>O<sub>3</sub> in the ancient black-glazed Jian (Tenmoku) wares. *Sci. Rep.* **4**, 4941 (2014).
- Forestier, H. & Guio-Quillain, G. First observation of a new iron (III) oxide. *C. R. Acad. Sci.* **199**, 720–723 (1934).
- Buttner, R. & Schrader, G. First measurements of Epsilon Ferrite XRD Powder Pattern. *Z. Anorg. Allg. Chem.* **320**, 220–234 (1963).
- Quemeneur, L. & Walter-Levy, E. Measurements of  $\epsilon$ -Fe<sub>2</sub>O<sub>3</sub> powder diffraction pattern. *C. R. Acad. Sci.* **257**, 3410–3413 (1963).
- Trautmann, J. M. & Forestier, H. First phase purity in  $\epsilon$ -Fe<sub>2</sub>O<sub>3</sub>. *C. R. Acad. Sci.* **261**, 4423–4425 (1965).
- Tronc, E., Chanéac, C. & Jolivet, J. P. Structural and Magnetic Characterization of  $\epsilon$ -Fe<sub>2</sub>O<sub>3</sub>. *J. Solid State Chem.* **139**, 93–104 (1998).
- Popovici, M. *et al.* Magnetic  $\epsilon$ -Fe<sub>2</sub>O<sub>3</sub> nanoparticles obtained by sol-gel synthesis. *Mater. Struct.* **13**, 79–81 (2006).
- Ohkoshi, S. *et al.* A millimeter-wave absorber based on gallium-substituted  $\epsilon$ -Fe<sub>2</sub>O<sub>3</sub> nanomagnets. *Angew. Chem. Int. Ed. Engl.* **46**, 8392–8395 (2007).
- Tseng, Y.-C. *et al.* Nonzero orbital moment in high coercivity  $\epsilon$ -Fe<sub>2</sub>O<sub>3</sub> and low-temperature collapse of the magnetocrystalline anisotropy. *Phys. Rev. B* **79**, 94404 (2009).



24. Yoshikiyo, M., Yamada, K., Namai, A. & Ohkoshi, S. Study of the Electronic Structure and Magnetic Properties of  $\varepsilon$ -Fe<sub>2</sub>O<sub>3</sub> by First-Principles Calculation and Molecular Orbital Calculations. *J. Phys. Chem. C* **116**, 8688–8691 (2012).
25. Chan, W. L., Deibel, J. & Mittleman, D. M. Imaging with terahertz radiation. *Reports Prog. Phys.* **70**, 1325 (2007).
26. Ferguson, B. & Zhang, X.-C. Materials for terahertz science and technology. *Nat. Mater.* **1**, 26–33 (2002).
27. Huber, R. *et al.* How many-particle interactions develop after ultrafast excitation of an electron-hole plasma. *Nature* **414**, 286–289 (2001).
28. Nuss, M. C. & Orenstein, J. In *Millimeter and Submillimeter Wave Spectroscopy of Solids* (ed. Grüner, G.) 7–50 (Springer Berlin Heidelberg), doi:[10.1007/BFb0103419](https://doi.org/10.1007/BFb0103419) (1998).
29. Nagel, M. *et al.* Integrated THz technology for label-free genetic diagnostics. *Appl. Phys. Lett.* **80**, 154–156 (2002).
30. Ohkoshi, S.-I. *et al.* Nanometer-size hard magnetic ferrite exhibiting high optical-transparency and nonlinear optical-magnetoelectric effect. *Scientific Reports* **5**, 14414 (2015).
31. Carraro, G. *et al.* Enhanced Hydrogen Production by Photoreforming of Renewable Oxygenates Through Nanostructured Fe<sub>2</sub>O<sub>3</sub> Polymorphs. *Adv. Funct. Mater.* **24**, 372–378 (2014).
32. Carraro, G. *et al.* Supported  $\varepsilon$  and  $\beta$  iron oxide nanomaterials by chemical vapor deposition; structure, morphology and magnetic properties. *Cryst Eng Comm* **15**, 1039–1042 (2013).
33. Gich, M. *et al.* Epitaxial stabilization of  $\varepsilon$ -Fe<sub>2</sub>O<sub>3</sub> (001) thin films on SrTiO<sub>3</sub> (111). *Appl. Phys. Lett.* **96**, 112508 (2010).
34. Gich, M. *et al.* Multiferroic Iron Oxide Thin Films at Room Temperature. *Adv. Mater.* **26**, 4645–4652 (2014).
35. Thai, T. M. N. *et al.* Stabilization of metastable  $\varepsilon$ -Fe<sub>2</sub>O<sub>3</sub> thin films using a GaFeO<sub>3</sub> buffer. *J. Appl. Phys.* **120**, 185304 (2016).
36. Trassin, M. *et al.* Epitaxial thin films of multiferroic GaFeO<sub>3</sub> on conducting indium tin oxide (001) buffered yttrium-stabilized zirconia (001) by pulsed laser deposition. *Appl. Phys. Lett.* **91**, 202504 (2007).
37. Lee, H. N. *et al.* Growth and characterization of non-*c*-oriented epitaxial ferroelectric SrBi<sub>2</sub>Ta<sub>2</sub>O<sub>9</sub> films on buffered Si (100). *Appl. Phys. Lett.* **77**, 3260–3262 (2000).
38. Jia, Q. X. *et al.* Epitaxial growth of highly conductive RuO<sub>2</sub> thin films on (100) Si. *Appl. Phys. Lett.* **68**, 1069–1071 (1996).
39. Jun, S., Kim, Y. S., Lee, J. & Kim, Y. W. Dielectric properties of strained (Ba, Sr)TiO<sub>3</sub> thin films epitaxially grown on Si with thin yttria-stabilized zirconia buffer layer. *Appl. Phys. Lett.* **78**, 2542–2544 (2001).
40. Momma, K. & Izumi, F. VESTA 3 for three-dimensional visualization of crystal, volumetric and morphology data. *J. Appl. Crystallogr.* **44**, 1272–1276 (2011).
41. Ohkoshi, S. & Tokoro, H. Hard Magnetic Ferrite:  $\varepsilon$ -Fe<sub>2</sub>O<sub>3</sub>. *Bull. Chem. Soc. Jpn.* **86**, 897–907 (2013).
42. Mukherjee, S. *et al.* Room temperature nanoscale ferroelectricity in magnetoelectric GaFeO<sub>3</sub> epitaxial thin films. *Phys. Rev. Lett.* **111**, 1–5 (2013).
43. Corbellini, L. *et al.* Analysis of hysteresis loops revisited – an easy method to separate contributions in ferromagnetic and ferroelectric measurements. *J. Appl. Phys.* **120**, 124101 (2016).
44. Wei, Y. *et al.* Synthesis of Fe<sub>3</sub>O<sub>4</sub> Nanoparticles and their Magnetic Properties. *Procedia Eng.* **27**, 632–637 (2012).
45. Angermann, A. & Töpfer, J. Synthesis of magnetite nanoparticles by thermal decomposition of ferrous oxalate dihydrate. *J. Mater. Sci.* **43**, 5123–5130 (2008).
46. Caruntu, D., Caruntu, G. & O'Connor, C. J. Magnetic properties of variable-sized Fe<sub>3</sub>O<sub>4</sub> nanoparticles synthesized from non-aqueous homogeneous solutions of polyols. *J. Phys. D: Appl. Phys.* **40**, 5801–5809 (2007).
47. Roca, A. G., Morales, M. P., O'Grady, K. & Serna, C. J. Structural and magnetic properties of uniform magnetite nanoparticles prepared by high temperature decomposition of organic precursors. *Nanotechnology* **17**, 2783–2788 (2006).
48. Yan, F., Li, J., Zhang, J., Liu, F. & Yang, W. Preparation of Fe<sub>3</sub>O<sub>4</sub>/polystyrene composite particles from monolayer oleic acid modified Fe<sub>3</sub>O<sub>4</sub> nanoparticles via miniemulsion polymerization. *J. Nanoparticle Res.* **11**, 289–296 (2009).
49. Coey, J. M. D. *Magnetism and Magnetic Materials*. (Cambridge University Press, 2010).
50. Sofin, R. G. S., Wu, H.-C. & Shvets, I. V. Anomalous magnetization reversal due to proximity effect of antiphase boundaries. *Phys. Rev. B* **84**, 212403 (2011).
51. Rigato, F., Geshev, J., Skumryev, V. & Fontcuberta, J. The magnetization of epitaxial nanometric CoFe<sub>2</sub>O<sub>4</sub>(001) layers. *J. Appl. Phys.* **106**, 113924 (2009).
52. Lacroix, C., Lambert-Milot, S., Desjardins, P., Masut, R. A. & Ménard, D. Adjusting the magnetic properties of semiconductor epilayers by the crystallographic orientation of embedded highly anisotropic magnetic nanoclusters. *J. Appl. Phys.* **105**, 07C119 (2009).
53. Lacroix, C., Lambert-Milot, S., Masut, R. A., Desjardins, P. & Ménard, D. Ferromagnetic resonance measurements of GaP epilayers with embedded MnP nanoclusters grown on GaP(001). *Phys. Rev. B - Condens. Matter Mater. Phys.* **87**, 1–10 (2013).
54. Lambert-Milot, S. *et al.* MnP nanoclusters embedded in GaP epitaxial films grown by organometallic vapor-phase epitaxy: A reciprocal space mapping and transmission electron microscopy study. *J. Vac. Sci. Technol. A* **30**, 61510 (2012).
55. Gauquelin, N. *et al.* Atomic scale real-space mapping of holes in YBa<sub>2</sub>Cu<sub>3</sub>O<sub>6</sub> +  $\delta$ . *Nat. Commun.* **5**, 4275 (2014).

## Acknowledgements

This work was supported by grants from the Natural Sciences and Engineering Research Council (NSERC - Canada) and the Fonds de recherche du Québec - Nature et technologies (FRQNT - Québec). Electron microscopy was carried out at the Canadian Centre for Electron Microscopy, a facility supported by the Canada Foundation for Innovation under the Major Science Initiative program, the NSERC and McMaster University. The authors acknowledge Julien Plathier of INRS – EMT for his help with the development and application of the D-D-SI technique to our magnetic measurements.

## Author Contributions

L.C. performed the growth of the  $\varepsilon$ -Fe<sub>2</sub>O<sub>3</sub> thin films, their x-ray diffractometry and magnetic characterization, and analyzed the obtained data. C.L., C.H., D.M. and A.P. participated in discussions on the analysis of the XRD and magnetic results. C.L. and D.M. developed the mathematical model to analyze the angular dependent magnetic measurements. A.K. and G.B. recorded the STEM images of the epsilon ferrite thin films and performed the multi-slice calculations of high-angle annular dark field (HAADF) images. L.C., A.P. and G.B. performed the analysis of the STEM images. L.C. wrote the manuscript with contribution from all authors.

## Additional Information

**Supplementary information** accompanies this paper at doi:[10.1038/s41598-017-02742-9](https://doi.org/10.1038/s41598-017-02742-9)

**Competing Interests:** The authors declare that they have no competing interests.

**Publisher's note:** Springer Nature remains neutral with regard to jurisdictional claims in published maps and institutional affiliations.



**Open Access** This article is licensed under a Creative Commons Attribution 4.0 International License, which permits use, sharing, adaptation, distribution and reproduction in any medium or format, as long as you give appropriate credit to the original author(s) and the source, provide a link to the Creative Commons license, and indicate if changes were made. The images or other third party material in this article are included in the article's Creative Commons license, unless indicated otherwise in a credit line to the material. If material is not included in the article's Creative Commons license and your intended use is not permitted by statutory regulation or exceeds the permitted use, you will need to obtain permission directly from the copyright holder. To view a copy of this license, visit <http://creativecommons.org/licenses/by/4.0/>.

© The Author(s) 2017